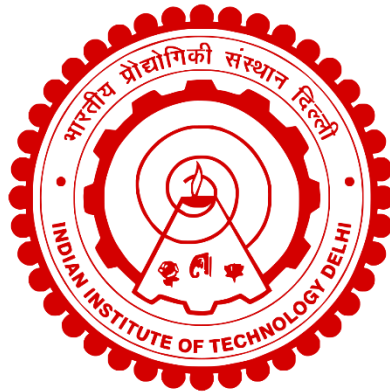


**STUDY OF PIEZOELECTRIC AND TRIBOELECTRIC
EFFECTS IN FLEXIBLE NANOCOMPOSITE FILMS**

ARUN MONDAL



**DEPARTMENT OF PHYSICS
INDIAN INSTITUTE OF TECHNOLOGY DELHI
DECEMBER 2024**

© Indian Institute of Technology Delhi (IITD), New Delhi, 2024

**STUDY OF PIEZOELECTRIC AND TRIBOELECTRIC
EFFECTS IN FLEXIBLE NANOCOMPOSITE FILMS**

by

ARUN MONDAL

Department of Physics

Submitted

**in fulfilment of the requirements of the degree of Doctor of Philosophy
to the**



**DEPARTMENT OF PHYSICS
INDIAN INSTITUTE OF TECHNOLOGY DELHI
DECEMBER 2024**

Dedicated

to

My Family

CERTIFICATE

This is to certify that the thesis entitled “**Study of Piezoelectric and Triboelectric Effects in Flexible Nanocomposite Films**”, being submitted by **Arun Mondal** to the Department of Physics, Indian Institute of Technology, Delhi, is worthy of consideration for the award of the degree of Doctor of Philosophy and is a record of the original bonafide research work carried out by him under my guidance and supervision. He has fulfilled all the criteria for the submission of the thesis, which is in my opinion has reached the necessary standard.

The results contained in this thesis have not been submitted, in part or full, to any other university or institute for the award of any degree/diploma.

Prof. Neeraj Khare

Department of Physics

Indian Institute of Technology Delhi

Hauz Khas, New Delhi-110016, India

ACKNOWLEDGEMENTS

I am deeply grateful to the “Almighty God” for my existence and all the blessings that have shaped my journey and always provided me with the strength and positivity to progress in life.

I extend my heartfelt appreciation to my respected supervisor, Prof. Neeraj Khare, whose invaluable guidance, motivation, and expertise have been instrumental in the completion of this work. His kindness and unwavering support have been a constant source of encouragement throughout the research process. The lessons I have learned from him will undoubtedly leave a lasting impact on my life.

I am grateful to the members of my Student Research Committee (SRC), Prof. Pankaj Srivastava, Prof. Jitendra Pratap Singh, and Prof. Bhaskar Mitra, for their diligent evaluation of my research progress at every stage and for offering valuable suggestions for improvement.

I extend my sincere appreciation to Prof. Sujeet Chaudhary, the Head of the Physics Department at IIT Delhi, for providing access to various research facilities. Furthermore, I would like to express my gratitude to the DRC chairperson of the Physics Department at IIT Delhi, for generously dedicating his time and offering support in overseeing the progress of my research work.

I also wish to express my sincere gratitude to Dr. Sangeeta Khare for generously sharing her experiences and knowledge with me. Her insights have enriched my understanding and contributed significantly to the success of this endeavour.

I also wish to thank the Nanoscale Research Facility (NRF), Central Research Facility (CRF), and all the technical staff of IIT Delhi for their assistance and provision of characterization facilities during the duration of my research.

I extend my heartfelt gratitude to my colleagues at the Nano Functional Oxides and Superconductivity Laboratory (NFOSL), including Dr. Mohd. Faraz, Dr. Deepanshu Sharma,

Dr. Sandeep Munjal, Dr. Surbhi Sharma, Dr. Satyendra Prakash Pal, Dr. Rohit Kumar, Dr. Sunil Kumar, Dr. Pratisha Gangwar, Dr. Huidrom Hemojit Singh, Dr. Dheeraj Kumar, Dr. Mamta Dahiya, Dr. Amish Kumar Gautam, Dr. Mohit Khosya, Dr. Birendra Kumar, Dr. Gaurav Sharma, Mrs. Abhilasha Chouksey, Mr. Aman Sharma, Mr. Gaurav Kumar, Mr. Manoj Singh, Mr. Sandeep Kumar, Ms. Rajni, and Ms. Sarita. Their support and contributions have been invaluable in creating a conducive working environment in the lab. I offer special thanks to Dr. Mohd. Faraz and Dr. Huidrom Hemojit Singh, for generously sharing their experiences, knowledge, constant motivation, and all the discussions, which have been particularly beneficial to me. From each labmate, I have gained valuable insights and knowledge. I extend my best wishes to all of them for success in their future endeavours.

I sincerely thank the M.Sc., M.Tech., and B.Tech. students with whom I collaborate for project works, for their invaluable support and engaging discussions.

I extend my gratitude to all my colleagues from the Student Affairs Council (SAC), IIT Delhi, for the tenure of 2022-23, as well as to the Deans of Student Affairs and all the staff for the valuable time and collaborative efforts we shared to served constructively for the IIT Delhi. I also express my gratitude to all my colleagues from the House Working Committee (HWC) of Nilgiri Hostel for the tenure of 2023-24 and also to the Warden, Caretaker, Mess supervisor and all other staff.

I deeply appreciate the unwavering support of my parents, Mr. Gopal Chandra Mondal and Mrs. Lalita Mondal, as well as my brother, Mr. Barun Mondal, and my sister-in-law, Mrs. Pallabi Mondal. I also want to share my deep love for my beloved nephew, Deeptayan Mondal. Their unconditional love, care, and encouragement have been indispensable throughout my journey. I owe my success to their constant backing, and I dedicate this thesis to my family as a token of gratitude.

I hold deep love and respect for my friends cum. seniors, Mr. Suvom Roy, Mr. Sourav Patranabish, Mr. Nadeem Tariq Beigh, Mr. Sumallya Mukhopadhyay, Mr. Arpan Malkhandi, Mr. Utkarsh Kumar, and Mr. Arup Anshuman. I also thank my beloved friends Mr. Krishnendu Ghorui, Ms. Prerna Joshi, Ms. Shreyashi Sinha, Ms. Puspita Chanda, Ms. Pratyusha Thakur, Ms. Subi Nath, Ms. Mouli Hazra, Ms. Soumidipa, Mr. Soham Das, Mr. Bibaswan Bose, Mr. Biswajit Saha, Mr. Tapabrata Pramanik, Mr. Dibyajyoti Mukherjee, Mr. Arunesh Singh, Mr. Subhajit Bhaskar, Mr. Dhananjay Mondal, Mr. Manoj Singh, Ms. Rajni, Ms. Simran Dhiman, Ms. Shivani Kumawat, Ms. Sonika Singh, Ms. Ekta Yadav, Ms. Neetesh Dhakar, Ms. Anupriya Tiwari, Mr. Indraneel Sinha, Ms. Arpita Mondal, Mr. Amit Rathore, Mr. Desh Deepak Gaur, Mr. Deepanshu Aggarwal, Mr. Anuj Singh, Mr. Yetendra Jha, Mr. Imran Khan, Ms. Rangeeta, Ms. Neesha Yadav, Ms. Kiran, Mr. Amit Mandal, Mr. Buddhadeb Mal, Mr. Samadarshi Mondal, Mr. Satwik, Acharya, Mr. Soumik Saha, Mr. Divyanshu Bujethia, Mr. Sunit Singh Rajput, Mr. Vishal Srivastava, Mr. Jyoti Rani Nath, Mr. Intaf Alam, Mr. Umang Chaturvedi, Mr. Hitesh for all the good memories throughout my Ph.D degree.

Finally, I sincerely acknowledge the financial support provided by the Ministry of Electronics and Information Technology (MeitY), the Department of Science and Technology (DST), India, as well as the Council of Scientific and Industrial Research (CSIR) for providing the Junior Research Fellowship (JRF) and Senior Research Fellowship (SRF) during my Ph.D. work.

Arun Mondal

ABSTRACT

In recent years, the demand for renewable energy has surged in the research community, driven by the necessity to power portable electronic devices sustainably and mitigate the environmental impact of fossil fuels. Mechanical vibrations offer a promising energy source for harvesting, leading to the emergence of nanogenerators. These devices, utilizing piezoelectricity and triboelectricity, convert mechanical energy from various sources into electricity. The present thesis focuses on enhancing the efficiencies of the nanogenerators by employing flexible polymer nanocomposites in both piezoelectric nanogenerators (PENGs) and triboelectric nanogenerators (TENGs) by tuning the material properties and external perturbations.

In order to investigate how internal material properties affect the electrical performance of Polyvinylidene Fluoride (PVDF) nanocomposite-based piezoelectric nanogenerators, simulations of PENG outputs have been carried out by finite elemental method (FEM) using COMSOL MULTIPHYSICS 5.5. The electrical outputs were simulated by adjusting parameters such as the piezoelectric coefficient (d_{33}) and dielectric constant (ϵ_r). The open-circuit voltage is found to be influenced by both d_{33} and ϵ_r , with the voltage increasing proportionally to d_{33} but decreasing inversely to ϵ_r . On the other hand, the short-circuit current is only influenced by d_{33} , increasing directly with it. Thus, optimizing the balance between these parameters is crucial for maximizing output. Experimental verification is performed using fabricated PVDF/NiO nanocomposite-based PENGs, showing close agreement between experimental and simulated results.

Further, magnetic cobalt ferrite (CoFe_2O_4) nanoparticles have been incorporated into the PVDF matrix for fabricating PENGs to improve the piezoelectric performances and investigate the influence of an external magnetic field on electrical performance. PENGs are fabricated using

5wt% and 10wt% CoFe₂O₄ nanoparticles in the PVDF matrix alongside pure PVDF for comparison. The PENG with 5wt% CoFe₂O₄ nanoparticles demonstrates the highest performance, with short-circuit currents and open-circuit voltages increasing by 1.5 times and 1.8 times, respectively, compared to pure PVDF. Under varying strengths of external magnetic fields (0 to 2.1 kGauss), short-circuit currents increase for both PVDF-5wt% CoFe₂O₄ and PVDF-10wt% CoFe₂O₄ PENGs. However, open-circuit voltage remains constant. Additionally, analysis of power density under different external loads reveals higher maximum power density with a lower external load in the presence of a 2.1 kGauss magnetic field, attributed to reduced internal resistance due to the alignment of magnetic dipoles induced by the field, which resulted in the enhanced performance.

In the next step, PVDF-based triboelectric nanogenerators have been fabricated to explore another mechanical energy harvesting technique and investigate the impact of ambient temperature on the TENG outputs to improve their efficiency. A homemade setup is designed to control the TENG's surrounding temperature, where the measurements are conducted at various temperatures (33°C, 35°C, 38°C, 41°C, 56°C, 70°C, and 84°C), revealing that both open-circuit voltages and short-circuit currents increase up to 41°C before declining with further temperature rise. The open-circuit voltage is found to increase from 6.2 V to 20 V with the increase in the ambient temperature up to 41°C, where an 11 times enhancement in the output power density of the TENG has been achieved at 41°C as compared to room temperature (33°C). Dielectric analysis shows that PVDF's relative permittivity increases with temperature, yet conductivity also rises, leading to surface charge loss. Beyond 41°C, the dominant effect shifts from dielectricity to conductivity, resulting in decreased electrical outputs due to reduced surface charges at higher temperatures, supported by transferred charge measurements. Furthermore, it explores the impact of fillers by incorporating CdS nanofillers into the PVDF

matrix, which boosts relative permittivity through interfacial polarizations, consequently enhancing electrical outputs compared to bare PVDF-based TENGs.

Finally, structural modification of the electronegative layers has been carried out to improve the electrical outputs of the TENGs by reducing the loss of surface charges and maximizing the surface charge generations during contact electrifications. The design involves double layer nanocomposite polymers: a bottom layer of PDMS incorporated with sodium niobate (NaNbO_3) nanoparticles and a top layer composed of a PVDF and MXene $\text{Ti}_3\text{C}_2\text{T}_x$ nanoparticles composite. Electrical measurements were conducted on TENGs with four different layer configurations: bare PVDF, PVDF/PDMS, PVDF/PDMS-15wt% NaNbO_3 nanocomposite (P/15NP), and (PVDF-15wt% $\text{Ti}_3\text{C}_2\text{T}_x$)/(PDMS-15wt% NaNbO_3) nanocomposite (15MP/15NP). The 15MP/15NP-based TENG exhibited remarkable performance improvements, achieving an enhancement of 1.9 times in open-circuit voltage, 2 times in short-circuit current, and 1.7 times in transferred charges compared to bare PVDF-based TENGs. 5.8 times increase in power density is observed in the 15MP/15NP configuration. Surface potential characterizations using KPFM revealed a reduction in surface potential with the addition of fillers, leading to an increased work function that aids charge transfer during contact electrification. The high dielectricity of NaNbO_3 improves internal polarization and reduces charge loss, while the high electronegativity of MXene facilitates charge transfer during contact electrification, thus enhancing the overall performance of the TENGs.

सार

हाल के वर्षों में, नवीकरणीय ऊर्जा की मांग शोध समुदाय में तेजी से बढ़ी है, जो वहनीय इलेक्ट्रॉनिक उपकरणों को टिकाऊ ढंग से ऊर्जा प्रदान करने और जीवाश्म ईंधन के पर्यावरणीय प्रभाव को कम करने की आवश्यकता से प्रेरित है। यांत्रिक कंपन ऊर्जा संचयन के लिए एक संभावित स्रोत प्रदान करता है, जिससे नैनोजेनेरेटर्स का उद्भव हुआ है। ये उपकरण पीज़ोइलेक्ट्रिसिटी और ट्राइबोइलेक्ट्रिसिटी का उपयोग करके विभिन्न स्रोतों से यांत्रिक ऊर्जा को विद्युत ऊर्जा में परिवर्तित करते हैं। प्रस्तुत शोध प्रबंध में पीज़ोइलेक्ट्रिक नैनोजेनेरेटर (PENGs) और ट्राइबोइलेक्ट्रिक नैनोजेनेरेटर (TENGs) में लचीले पॉलिमर नैनोकंपोज़िट्स का उपयोग करके इनकी दक्षता बढ़ाने पर ध्यान केंद्रित किया गया है, जिसमें सामग्री के गुणों और बाहरी प्रभावों को समायोजित किया गया है।

पॉलीविनाइलिडीन फ़्लोराइड (PVDF) नैनोकंपोज़िट-आधारित पीज़ोइलेक्ट्रिक नैनोजेनेरेटर्स के विद्युत प्रदर्शन पर आंतरिक सामग्री गुणों के प्रभाव की जांच करने के लिए COMSOL MULTIPHYSICS 5.5 का उपयोग करके सीमित तत्व विधि (FEM) द्वारा PENG के उत्पादन का अनुकरण किया गया है। पीज़ोइलेक्ट्रिक गुणांक (d_{33}) और डायलेक्ट्रिक स्थिरांक (ϵ_r) जैसे मापदंडों को समायोजित करके विद्युत उत्पादन का अनुकरण किया गया। पाया गया कि ओपन-सर्किट वोल्टेज d_{33} के साथ सीधे अनुपात में बढ़ता है, लेकिन ϵ_r के विपरीत अनुपात में घटता है। दूसरी ओर, शॉर्ट-सर्किट करंट केवल d_{33} से प्रभावित होता है, जो इसके साथ सीधे बढ़ता है। इसलिए, इन मापदंडों के बीच संतुलन अनुकूलित करना उत्पादन को अधिकतम करने के लिए महत्वपूर्ण है। PVDF/NiO नैनोकंपोज़िट-आधारित PENGs का उपयोग करके किए गए प्रयोगात्मक सत्यापन ने अनुकरण और प्रयोगात्मक परिणामों के बीच निकटता को दर्शाया गया।

इसके अलावा, पीज़ोइलेक्ट्रिक प्रदर्शन में सुधार के लिए PVDF मैट्रिक्स में मैग्नेटिक कोबाल्ट फेराइट (CoFe_2O_4) नैनोकणों को शामिल किया गया है और बाहरी चुंबकीय क्षेत्र का विद्युत प्रदर्शन पर प्रभाव

जांचा गया है। तुलना के लिए 5wt% और 10wt% CoFe_2O_4 नैनोकणों के साथ PVDF मैट्रिक्स में PENGs बनाए गए हैं। 5wt% CoFe_2O_4 नैनोकणों वाले PENG ने सबसे अच्छा प्रदर्शन किया, जिसमें शॉर्ट-सर्किट करंट और ओपन-सर्किट वोल्टेज क्रमशः शुद्ध PVDF की तुलना में 1.5 गुना और 1.8 गुना बढ़े। बाहरी चुंबकीय क्षेत्र की विभिन्न ताकतों (0 से 2.1 kGauss) के तहत, PVDF-5wt% CoFe_2O_4 और PVDF-10wt% CoFe_2O_4 PENGs के लिए शॉर्ट-सर्किट करंट बढ़े, लेकिन ओपन-सर्किट वोल्टेज स्थिर रहा। बाहरी लोड पर विभिन्न परिस्थितियों में शक्ति घनत्व के विश्लेषण से पता चला कि 2.1 kGauss चुंबकीय क्षेत्र की उपस्थिति में कम बाहरी लोड के साथ उच्चतम शक्ति घनत्व प्राप्त हुई, जो चुंबकीय क्षेत्र द्वारा प्रेरित चुंबकीय द्विध्रुवों के संरेखण के कारण आंतरिक प्रतिरोध में कमी के कारण प्रदर्शन में वृद्धि के लिए जिम्मेदार है।

अगले चरण में, एक अन्य यांत्रिक ऊर्जा संचयन तकनीक का पता लगाने और TENGs की दक्षता में सुधार के लिए परिवेश के तापमान के प्रभाव की जांच हेतु PVDF-आधारित ट्राइबोइलेक्ट्रिक नैनोजेनेरेटर्स का निर्माण किया गया है। घर के बने ढाँचे को TENG के आसपास के तापमान को नियंत्रित करने के लिए रूपांकित किया गया, जहाँ विभिन्न तापमानों (33°C, 35°C, 38°C, 41°C, 56°C, 70°C, और 84°C) पर माप किए गए। परिणामस्वरूप, पाया गया कि 41°C तक दोनों ओपन-सर्किट वोल्टेज और शॉर्ट-सर्किट करंट बढ़ते हैं, लेकिन इसके बाद तापमान में वृद्धि के साथ ये घटने लगते हैं। ओपन-सर्किट वोल्टेज 6.2 V से बढ़कर 20 V हो गया, जिसमें तापमान 41°C तक बढ़ा। परिवेश के तापमान (33°C) की तुलना में 41°C पर TENG की उत्पादन शक्ति घनत्व में 11 गुना वृद्धि प्राप्त की गई। डायलेक्ट्रिक विश्लेषण से पता चला कि तापमान के साथ PVDF की सापेक्षता पारगम्यता बढ़ती है, फिर भी चालकता भी बढ़ जाती है, जिससे सतह आवेश की हानि होती है। 41°C के बाद, प्रमुख प्रभाव चालकता में स्थानांतरित हो जाता है, जिसके परिणामस्वरूप उच्च तापमान पर सतह आवेश में कमी के कारण विद्युत उत्पादन घटते हैं, जिसे स्थानांतरित आवेश माप से समर्थन प्राप्त हुआ। इसके अलावा, PVDF मैट्रिक्स में CdS नैनोफिलर्स को

शामिल करने के प्रभावों की जांच की गई, जिससे अंतरफलक ध्रुवीकरण के माध्यम से सापेक्ष पारगम्यता में वृद्धि हुई, और इस प्रकार विद्युत उत्पादन में शुद्ध PVDF-आधारित TENGs की तुलना में वृद्धि हुई। अंत में, TENGs के विद्युत उत्पादन को बेहतर बनाने के लिए विद्युतीकरण के दौरान सतह आवेश की हानि को कम करने और सतह आवेश उत्पन्न करने को अधिकतम करने के लिए विद्युत ऋणात्मक परतों का संरचनात्मक संशोधन किया गया है। बनावट में दोहरी परत नैनोकंपोज़िट पॉलिमर शामिल हैं: PDMS का एक निचला स्तर जिसमें सोडियम नाइओबेट (NaNbO_3) नैनोकण शामिल हैं और एक शीर्ष स्तर जिसमें PVDF और MXene $\text{Ti}_3\text{C}_2\text{T}_x$ नैनोकण कंपोज़िट शामिल है। चार विभिन्न परत विन्यास वाले TENGs पर विद्युत माप किए गए: शुद्ध PVDF, PVDF/PDMS, PVDF/PDMS-15wt% NaNbO_3 नैनोकंपोज़िट (P/15NP), और (PVDF-15wt% $\text{Ti}_3\text{C}_2\text{T}_x$)/(PDMS-15wt% NaNbO_3) नैनोकंपोज़िट (15MP/15NP)। 15MP/15NP-आधारित TENG ने उल्लेखनीय प्रदर्शन सुधार हासिल किया, जिसमें ओपन-सर्किट वोल्टेज में 1.9 गुना, शॉर्ट-सर्किट करंट में 2 गुना, और स्थानांतरित आवेश में 1.7 गुना वृद्धि हुई। शुद्ध PVDF-आधारित TENGs की तुलना में शक्ति घनत्व में 5.8 गुना वृद्धि देखी गई। KPFM का उपयोग करके सतह संभावित विश्लेषण ने दिखाया कि फिलर्स के अतिरिक्त से सतह संभावित में कमी आई, जिससे कार्य फलन में वृद्धि हुई जो संपर्क विद्युतीकरण के दौरान आवेश हस्तांतरण में सहायक है। NaNbO_3 की उच्च पारगम्यता ने आंतरिक ध्रुवीकरण में सुधार किया और आवेश हानि को कम किया, जबकि MXene की उच्च विद्युत ऋणात्मकता ने संपर्क विद्युतीकरण के दौरान आवेश हस्तांतरण को सुगम बनाया, जिससे TENGs के कुल प्रदर्शन में सुधार हुआ।

TABLE OF CONTENTS

CERTIFICATE	i
ACKNOWLEDGMENTS	ii
ABSTRACT	v
TABLE OF CONTENTS	xi
LIST OF FIGURES	xvi
LIST OF TABLES	xxiv
CHAPTER 1: Introduction	1-38
1.1. Overview.....	1
1.2. Nanogenerator.....	3
1.2.1. Piezoelectric Nanogenerator	3
1.2.1.1. Basic Theory of Piezoelectricity	4
1.2.1.2. Design of Piezoelectric Nanogenerator.....	8
1.2.2. Triboelectric Nanogenerator	9
1.2.2.1. Basic Theory of Triboelectricity	10
1.2.2.2. Design of Triboelectric Nanogenerator.....	13
1.3. COMSOL MULTIPHYSICS	18
1.4. Main Challenges and Strategies of the Thesis	18
1.4.1. Choice of Polymers for Nanogenerators	21
1.4.1.1. Polyvinylidene Fluoride (PVDF)	21
1.4.1.2. Polydimethylsiloxane (PDMS)	22
1.4.2. Choice of Nanofillers	23
1.4.2.1. Cobalt Ferrite (CoFe ₂ O ₄)	23
1.4.2.2. Nickel Oxide (NiO)	24
1.4.2.3. Cadmium Sulfide (CdS)	25
1.4.2.4. MXene (Ti ₃ C ₂ T _x).....	26
1.4.2.5. Sodium Niobate (NaNbO ₃)	27
1.5. Motivation of the Thesis	28
1.6. Objectives of the Present Thesis	29
1.7. Outline of the Thesis.....	30

References.....	35
-----------------	----

CHAPTER 2: Experimental and Characterization Techniques **39-63**

2.1. Introduction.....	39
2.2. Synthesis Methods of Nanostructured Materials	40
2.2.1. Auto-Combustion Method	40
2.2.2. Hydrothermal Method.....	41
2.2.3. Chemical Exfoliation	42
2.3. Films and Electrodes Deposition	43
2.3.1. Drop-Casting Method	43
2.3.2. Spin-Coating Method.....	44
2.3.3. Electron-Beam Evaporation Technique	45
2.4. Fabrication of Piezoelectric and Triboelectric Nanogenerators.....	46
2.5. Characterization Techniques.....	48
2.5.1. X-ray Diffraction.....	48
2.5.2. Scanning Electron Microscopy	50
2.5.3. Energy Dispersive X-ray Spectroscopy	51
2.5.4. Transmission Electron Microscopy.....	52
2.5.5. Fourier Transform Infrared Spectroscopy.....	54
2.5.6. Polarization-Electric Field Loop Measurements.....	55
2.5.7. Dielectric Measurements.....	56
2.5.8. Scanning Probe Microscopy	57
2.5.8.1. Atomic Force Microscopy	57
2.5.8.2. Piezoresponse Force Microscopy	59
2.5.8.3. Kelvin Probe Force Microscopy	60
2.5.9. Electrical Measurements	61
References.....	63

CHAPTER 3: Experimental and Simulation Study of PVDF Nanocomposite-based Piezoelectric Nanogenerators **64-92**

3.1. Introduction.....	64
3.2. Theoretical Study of PENGs Using FEM.....	65
3.2.1. Structural parameters of the PENG Model.....	65
3.2.2. Effect of the Shape of External Force.....	66

3.2.3.	Variation of Output Voltage with External Loads	68
3.2.4.	Effect of d_{33} and ϵ_r on PENG Outputs	69
3.3.	Experimental Measurements of PENGs and Comparison with Simulated Results.....	72
3.3.1.	Synthesis of NiO Nanoparticles	73
3.3.2.	Fabrication of PVDF/NiO Nanocomposite Films	74
3.3.3.	Fabrication of PVDF/NiO Nanocomposite-based Piezoelectric Nanogenerator Devices	75
3.3.4.	Structural and Morphological Analysis of NiO Nanoparticles.....	75
3.3.5.	XRD Analysis of PVDF/NiO Nanocomposite Films	76
3.3.6.	FTIR Analysis of Nanocomposite Films	77
3.3.7.	Polarization-Electric Field Measurements of Nanocomposite Films	78
3.3.8.	Dielectric Analysis of the Nanocomposite Films	79
3.3.9.	PFM Analysis of Nanocomposite Films	81
3.3.10.	Electrical Measurements of the PVDF Nanocomposite-based PENGs.....	82
3.3.11.	Simulation of the PVDF/NiO Nanocomposite-based PENGs Using COMSOL MULTIPHYSICS.....	85
3.4.	Simulation of other Published Experimental Works.....	88
3.5.	Conclusions.....	89
	References.....	91

CHAPTER 4: Flexible PVDF/CoFe₂O₄ Nanocomposite Film-based Piezoelectric Nanogenerators for Improved Piezoresponses 93-111

4.1.	Introduction.....	93
4.2.	Experimental Section.....	94
4.2.1.	Synthesis of CoFe ₂ O ₄ Nanoparticles.....	95
4.2.2.	Fabrication of PVDF/CFO Nanocomposite Films.....	96
4.2.3.	Fabrication of PENG Devices.....	97
4.3.	Results and Discussions.....	97
4.3.1.	Structural and Morphological Analysis of CFO Nanoparticles	97
4.3.2.	Magnetization–Magnetic Field Analysis of CFO Nanoparticles	98
4.3.3.	Structural Phase Analysis of PVDF/CFO Nanocomposite Films	99
4.3.4.	Fourier Transform Infrared Spectroscopy (FTIR) Analysis of the Nanocomposite Films.....	100
4.3.5.	Polarization-Electric Field Measurements of Nanocomposite Films	101

4.3.6.	Magnetization–Magnetic Field Analysis of Nanocomposite Films.....	103
4.3.7.	Electrical Measurements of the PENGs.....	103
4.3.7.1.	Significance of CFO Filler Contents in PVDF on PENG Outputs ...	104
4.3.7.2.	Effect of External Magnetic Fields on PENG Outputs.....	105
4.3.8.	Mechanism Behind the Enhancements in PENG Outputs with External Magnetic Fields.....	109
4.4.	Conclusions.....	110
	References.....	111

CHAPTER 5: Effect of Ambient Temperature on the Performance of PVDF-based Triboelectric Nanogenerator **112-129**

5.1.	Introduction.....	112
5.2.	TENG Device Configuration and Measurement Setup.....	113
5.3.	Temperature Dependent PVDF-based TENG Performances.....	115
5.4.	Mechanism of the Temperature Dependent TENG Performances	117
5.5.	Temperature Dependent Study of PVDF/CdS Nanocomposite-based TENG.....	121
5.5.1.	Preparation of CdS Nanoparticles and PVDF/CdS Nanocomposite Films.....	122
5.5.2.	Structural and Morphological Analysis of CdS Nanoparticles	122
5.5.3.	Structural Phase Characterization of the PVDF/CdS nanocomposite	123
5.5.4.	Performances of PVDF/CdS nanocomposite-based TENG	124
5.6.	Conclusions.....	128
	References.....	129

CHAPTER 6: Flexible Polymer Nanocomposite Film-based Triboelectric Nanogenerators for Improved Electrical Performances **130-158**

6.1.	Introduction.....	130
6.2.	Experimental Section.....	132
6.2.1.	Synthesis of MXene ($Ti_3C_2T_x$) Nanoparticles	132
6.2.2.	Synthesis of $NaNbO_3$ Nanoparticles	133
6.2.3.	Fabrication of Electronegative Double-Layer Films	133
6.2.4.	Fabrication of the TENG Devices.....	134
6.3.	Results and Discussions.....	136
6.3.1.	Structural Phase Analysis of MAX Phase and MXene	136
6.3.2.	FESEM Micrograph of MXene for Morphological Analysis	137

6.3.3. Fourier Transform Infrared Spectroscopy of MXene	138
6.3.4. Structural Phase and Morphological Analysis of NaNbO ₃ Nanoparticles	139
6.3.5. Cross-sectional SEM Micrograph and Elemental Mapping of Double-Layer Structured Film	140
6.3.6. Electrical Measurements of TENG Devices	141
6.3.7. Kelvin Probe Force Microscopy Analysis	146
6.3.8. Dielectric Properties of the Double-Layered Films	148
6.4. Mechanism Behind the Performance of Triboelectric Nanogenerators	150
6.5. Applications of the TENGs for Wireless Communication Systems	154
6.6. Conclusions.....	155
References.....	157
CHAPTER 7: Conclusions and Future Scope	159-164
7.1. Conclusions of the Thesis	159
7.1.1. Experimental and Simulation Study of PVDF Nanocomposite-based Piezoelectric Nanogenerators.....	159
7.1.2. Flexible PVDF/CoFe ₂ O ₄ Nanocomposite Film-based Piezoelectric Nanogenerators for Improved Piezoresponses	160
7.1.3. Effect of Ambient Temperature on the PVDF-based Triboelectric Nanogenerator	161
7.1.4. Flexible Polymer Nanocomposite Film-based Triboelectric Nanogenerators for Improved Electrical Performances.....	163
7.2. Future Scope of the Thesis.....	164

LIST OF FIGURES

S. No.	Chapter 1	Page No.
Figure 1.1	Schematic representation of (a) direct piezoelectric effect and (b) reverse piezoelectric effect.	4
Figure 1.2	Crystal structure of a piezoelectric crystal, when (a) no external force is present, (b) external force is present and deformed the crystal. (c) The overall internal polarization developed due to the external force, and (d) the electrical signal across the piezoelectric material.	6
Figure 1.3	Tensor directions to indicate the consecutive relations.	8
Figure 1.4	(a) Single ZnO nanowire-based piezoelectric nanogenerator [34], (b) piezoelectric nanogenerator with interdigitated electrode [38], and (c) sandwich structure piezoelectric nanogenerator [39].	9
Figure 1.5	The schematic representation of the electron transfer during contact electrification by surface state model for metal and dielectric (a) before contact, (b) in contact, (c) after contact, and (d) charge release process at higher temperature (T_2). Here, (E_{VAC}) is the vacuum level; (E_C) represents the conduction band; (E_V) is the valence band; (E_n) refers to neutral level of surface states; ($f(E)$) denotes the Fermi-Dirac distribution probability [40].	11
Figure 1.6	The schematic representation of the electron transfer during contact electrification by electron cloud model for two dielectrics, (a) before contact, (b) in contact, (c) after contact, and (d) charge release process at higher temperature (T) once kT is greater than the potential barrier of the following material. Here, k is the Boltzmann constant, and d is the separation between material A and B [40].	12
Figure 1.7	The four operating modes of triboelectric nanogenerators are (a) vertical contact-separation mode, (b) lateral sliding mode, (c) single electrode mode, and (d) freestanding triboelectric layer mode.	14
Figure 1.8	Operating principle of TENG in contact-separation mode for Kapton and PMMA (a) before contact, (b) first contact, (c) releasing process, (d) fully released, (e) further pressing, and (f) The generation and reduction of the voltage signal with the pressing and releasing process, respectively, are plotted with time (s) [24].	15

Figure 1.9	The schematic model of (a) dielectric-to-dielectric, (b) dielectric-to-conductor contact separation mode TENG for the theoretical insight, and (c) the equivalent capacitive model [41].	17
Figure 1.10	Different polymorphic phases of PVDF [72].	22
Figure 1.11	The chemical structure of PDMS [74].	23
Figure 1.12	The crystal structure of the spinal cobalt ferrite [77].	24
Figure 1.13	The crystal structure of nickel oxide (NiO) [83].	25
Figure 1.14	The crystal structure of cadmium sulfide (CdS) [85].	26
Figure 1.15	Schematic representation of the MAX phase (Ti_3AlC_2) and MXene ($Ti_3C_2T_X$).	27
Figure 1.16	The crystal structure of cubic and orthorhombic phase of $NaNbO_3$ [96].	28

S. No.	Chapter 2	Page No.
Figure 2.1	Photograph of the auto-combustion synthesis method.	41
Figure 2.2	(a) Photograph of the autoclave with Teflon liner and (b) hot-air oven.	42
Figure 2.3	Schematic representation of the chemical exfoliation for the synthesis of layered material from bulk sample.	43
Figure 2.4	(a) Schematic representation and (b) photograph of spin-coater.	45
Figure 2.5	(a) Schematic representation of the setup inside the e-beam deposition chamber, (b) e-beam evaporation deposition system, and (c) inside view of the deposition chamber.	46
Figure 2.6	Schematic representations of the fabrication process of (a) piezoelectric nanogenerators and (b) triboelectric nanogenerators.	47
Figure 2.7	(a) Schematic representation of the X-ray diffraction followed by the Bragg's diffraction law, (b) XRD characterization unit <i>Rigaku, Ultima-IV</i> , and (c) components inside the sample chamber.	49
Figure 2.8	Schematic representation of the components of scanning electron microscope.	51
Figure 2.9	Schematic representation of the electron-samples interaction at the atomic level.	52

Figure 2.10	(a) Schematic representation of the components inside transmission electron microscopy and (b) photograph of the <i>JM-1400 (JEOL)</i> TEM system.	53
Figure 2.11	Schematic representation of the working inside the Fourier transform infrared spectroscopy.	55
Figure 2.12	(a) Schematic representation of the Sawyer-Tower circuit and (b) photograph of the P–E loop system <i>Precision Premier II</i> from Radiant Technologies.	56
Figure 2.13	Schematic representation of the (a) variation in the interaction force between the tip and the sample with their inter-separation and (b) working setup of the atomic force microscopy, (c), (d), and (e) Photographs of the <i>Bruker Dimension Icon</i> AFM setup.	58
Figure 2.14	Schematic representation of the working of piezoresponse force microscope, when the sample is under (a) no strain, (b) tensile strain, and (c) compressive strain.	60
Figure 2.15	Schematic representation of the energy levels for the tip and the sample when they are (a) separated, (b) made contact, and (c) external bias applied.	61

S. No.	Chapter 3	Page No.
Figure 3.1	Schematic representation of the piezoelectric nanogenerator, in which a PVDF nanocomposite film is sandwiched between two metal electrodes and electrical connections are made through a load resistance.	66
Figure 3.2	(a) Architecture of different forces such as sinusoidal, triangular, square, and sawtooth, and corresponding (b) open-circuit voltage, and (c) short-circuit current on the application of different shape of external forces.	67
Figure 3.3	(a) Variation in the shape of the square wave force with the variation of transition rate from minima-to-maxima of the force curve and inset shows a zoom part of the edge of force curve and (b) the variation of the open-circuit voltage and short-circuit current with the variation of the width of transition from minima to maxima.	68
Figure 3.4	Simulated PENG output voltage with the variation of external load resistances for $d_{33} = 40$ pC/N and 80 pC/N at fixed ϵ_r of (a) 8 and (b) 32.	69

Figure 3.5	Variation of (a) open-circuit voltage and (b) short-circuit current obtained for PVDF nanocomposite film-based PENG with different d_{33} when relative permittivity is kept constant at $\epsilon_r = 8$.	70
Figure 3.6	(a) Open-circuit voltage, (b) short-circuit current for different relative permittivity when d_{33} is kept constant at 80 pC/N, and (c) variation of open-circuit voltage with the ratio (d_{33}/ϵ_r).	72
Figure 3.7	Schematic representation of the steps followed for synthesizing nickel oxide (NiO) nanoparticles by auto-combustion method.	73
Figure 3.8	Schematic representation of the process steps followed for the synthesis of PVDF-NiO nanocomposite films.	74
Figure 3.9	(a) XRD pattern and (b) TEM image of NiO nanoparticles.	75
Figure 3.10	XRD pattern of the bare PVDF and PVDF-based nanocomposite films.	76
Figure 3.11	(a) FTIR spectra and (b) zoom part of FTIR spectra shows redshift of the peaks for PVDF-NiO nanocomposite as compared to bare PVDF.	77
Figure 3.12	Polarization-Electric field (P-E) loop curves of bare PVDF and PVDF/NiO nanocomposite films.	79
Figure 3.13	(a) Relative permittivity, (b) dielectric tangent loss ($\tan \delta$), and (c) measured ac conductivity of bare PVDF and PVDF-NiO nanocomposite films.	81
Figure 3.14	Variation of (a) PFM amplitude and (b) PFM phase with applied voltage for bare PVDF and PVDF/NiO nanocomposites.	82
Figure 3.15	(a) Open-circuit voltage and (b) short-circuit current of bare PVDF and PVDF/NiO nanocomposite-based piezoelectric nanogenerator.	83
Figure 3.16	(a) Resistance dependence output voltage and power density and (b) charging of 10 μ F and 47 μ F capacitors with PVDF/NiO (5 wt%) nanocomposite-based piezoelectric nanogenerator.	84
Figure 3.17	Theoretical results of (a) open-circuit voltage, (b) short-circuit current of PVDF/NiO nanocomposite-based pengs simulated by COMSOL MULTIPHYSICS. (c) Comparison between experimental and simulated results for output voltages and currents with different filler percentages.	86

S. No.	Chapter 4	Page No.
Figure 4.1	Schematic representation of the process steps followed for the synthesis of CFO nanoparticles.	95
Figure 4.2	Schematic representation of the process step followed for the fabrication of PVDF-CFO nanocomposite film by drop-casting method.	96
Figure 4.3	Schematic representation of the PVDF-CFO nanocomposite-based PENG device.	97
Figure 4.4	(a) XRD pattern and (b) TEM image of CFO nanoparticles.	98
Figure 4.5	Magnetization–Magnetic field (M-H) loop of CFO nanoparticles.	99
Figure 4.6	X-ray diffraction (XRD) pattern of bare PVDF, PVDF-5wt% CFO, and PVDF-10wt% CFO nanocomposite films.	100
Figure 4.7	Fourier transform infrared (FTIR) spectroscopy curves of bare PVDF, PVDF-5wt% CFO, and PVDF-10wt% CFO nanocomposite films.	101
Figure 4.8	Polarization–Electric field (P-E) loop of bare PVDF, PVDF-5wt% CFO, and PVDF-10wt% CFO nanocomposite films.	102
Figure 4.9	Magnetization–Magnetic field (M-H) loop of PVDF-5wt% CFO and PVDF-10wt% CFO nanocomposite films.	103
Figure 4.10	(a) Short-circuit current and (b) open-circuit voltage of bare PVDF, PVDF-5wt% CFO, and PVDF-10wt% CFO nanocomposite film-based PENGs.	104
Figure 4.11	(a) Short-circuit currents and (b) open-circuit voltages for PVDF-5wt% CFO, while (c) short-circuit currents and (d) open-circuit voltages for PVDF-10wt% CFO nanocomposite based PENGs in the presence of different external magnetic fields.	106
Figure 4.12	Charging of a 10 μ F capacitor with PVDF-5wt% CFO nanocomposite-based PENG when external magnetic field $H = 0$ and 2.1 kGauss.	107
Figure 4.13	(a) Output voltage and (b) output power density of the PVDF-5wt% CFO-based PENG in the absence and presence of the external magnetic field. (c) The variation of load resistance corresponds to the maximum power density delivered by PENG under the external magnetic field for PVDF-5wt% CFO nanocomposites. (d) The bar plot for the maximum power density corresponds to bare PVDF and	108

	PVDF-5wt% CFO nanocomposite-based PENG at $H = 0$ and 2.1 kGauss.	
Figure 4.14	A schematic representation of the mechanism behind the enhancement of PENG short-circuit current in the presence of the external magnetic field.	110

S. No.	Chapter 5	Page No.
Figure 5.1	The schematic representation of (a) PVDF film-based triboelectric nanogenerator (TENG) device and (b) measurement setup.	115
Figure 5.2	The variation of (a) V_{OC} and (b) I_{SC} with the ambient temperature for PVDF-based TENG plotted with time, (c) the maximum voltage and current plotted with ambient temperature. Variation of (d) output voltage, (e) output power density across different external loads, and (f) 10 μ F capacitor charging with the TENG at two different ambient temperatures of 33°C and 41°C.	117
Figure 5.3	(a) Frequency-dependent relative permittivity at different temperatures (dielectric loss in the inset), variation of (b) relative permittivity, (c) conductivity, and (d) transferred charges (Q_{TR}) with the temperature for the PVDF film.	121
Figure 5.4	(a) XRD spectra and (b) TEM image of the CdS nanoparticles.	123
Figure 5.5	XRD pattern of PVDF/CdS nanocomposite film.	123
Figure 5.6	The variations of (a) V_{OC} , (b) I_{SC} with the ambient temperature for PVDF/CdS nanocomposite-based TENG plotted at time scale, and (c) the maximum voltage and current plotted with ambient temperature. (d) The change in transferred charges with the ambient temperature.	124
Figure 5.7	(a) FTIR and (b) P-E loop spectra for bare PVDF and PVDF/CdS nanocomposite.	127

S. No.	Chapter 6	Page No.
Figure 6.1	The schematic representation of the synthesis of MXene	132
Figure 6.2	Schematic representations of the (a) TENG setup, different configurations of the electronegative layers, (b) bare PVDF, (c)	135

	PVDF/PDMS, (d) PVDF/PDMS-x wt% of NaNbO ₃ (P/xNP), and (e) PVDF-y wt% of MXene/PDMS-x wt% of NaNbO ₃ (yMP/xNP).	
Figure 6.3	(a) XRD pattern and (b) zoom image of peak shifting of XRD pattern for MAX phase and MXene exhibiting a shift in peak corresponding to (002) plane.	136
Figure 6.4	(a) FESEM image of MXene (Ti ₃ C ₂ T _X). EDS elemental mapping of (b–e) MAX phase (Ti ₃ AlC ₂) and (f–k) MXene (Ti ₃ C ₂ T _X).	138
Figure 6.5	Fourier transform infrared spectroscopy curve of MXene (Ti ₃ C ₂ T _X).	139
Figure 6.6	(a) XRD pattern and (b) SEM image of NaNbO ₃ nanoparticles.	140
Figure 6.7	Cross-sectional (a) SEM image and (b-g) the EDS mapping of the PVDF-15 wt% of MXene/PDMS-15 wt% of NaNbO ₃ (15MP/15NP) sample.	141
Figure 6.8	(a) Open-circuit voltages as a function of time, (b) bar plot of open-circuit voltages, (c) short-circuit currents as a function of time, (d) bar plot of short-circuit currents, (e) transferred charges as a function of time, and (f) bar plot of transferred charges for the bare PVDF, and electronegative double-layered TENGs. The “*” and “#” defines TENG outputs of PVDF/PDMS-15 wt% of NaNbO ₃ (P/15NP) and PVDF-15 wt% of MXene/PDMS-15 wt% of NaNbO ₃ (15MP/15NP), respectively in (b), (d), and (f).	143
Figure 6.9	(a) Output voltage and (b) power density for bare PVDF and 15MP/15NP-based TENGs. (c) A 1 μF capacitor charging with bare PVDF and 15MP/15NP based TENGs and (d) lighted-up 5 LEDs using 15MP/15NP based TENG.	144
Figure 6.10	The KPFM images for surface potential distribution for (a) copper plate, (b) bare PVDF, (c) PVDF/PDMS, (d) PVDF/PDMS-15 wt% of NaNbO ₃ (P/15NP), and (e) PVDF-15 wt% of MXene/PDMS-15 wt% of NaNbO ₃ (15MP/15NP), respectively. (f) Comparative potential distribution for all samples. (g) The schematic representation of the charge transfer between electropositive copper and electronegative double layers due to the difference in their work function.	147
Figure 6.11	Variation of (a) relative permittivity and (b) dielectric tangent loss with frequency for bare PVDF, PVDF/PDMS, PVDF/PDMS-15 wt% of NaNbO ₃ (P/15NP), and PVDF-15 wt% of MXene/PDMS-15 wt% of NaNbO ₃ (15MP/15NP).	149
Figure 6.12	(a) Decay of transferred charges with time for bare PVDF and 15MP/15NP film, inset of the figure shows the percentage of charges	151

	retained after 20 sec on bare PVDF, PVDF/PDMS, PVDF/PDMS-15 wt% of NaNbO ₃ (P/15NP), and PVDF-15 wt% of MXene/PDMS-15 wt% of NaNbO ₃ (15MP/15NP), (b) P-E loop of the bare PVDF, PVDF/PDMS, and PVDF/PDMS-NaNbO ₃ nanocomposites, and (c) FTIR spectra of the bare PVDF and the PVDF-MXene nanocomposites.	
Figure 6.13	The mechanism behind the (a) charge loss in bare PVDF, (b) improvement of charge storing at the interface of PVDF and PDMS in PVDF/PDMS film, (c) generation of internal polarizations due to the incorporation of NaNbO ₃ in PDMS in PVDF/PDMS-x wt% of NaNbO ₃ (P/xNP) film, and (d) improved surface charge generation due to the presence of MXene in PVDF in PVDF-y wt% of MXene/PDMS-x wt% of NaNbO ₃ (yMP/xNP).	153
Figure 6.14	(a) The schematic representation and (b) photograph of the wireless communication system using TENG.	155

LIST OF TABLES

S. No.	Chapter 3	Page No.
Table 3.1	Comparison of open-circuit voltage of the PVDF/NiO nanocomposite-based PENGs with previous reports	84
Table 3.2	Comparison between experimental and simulated results for open-circuit voltage and short-circuit current for bare PVDF, PVDF/NiO (5 wt%), and PVDF/NiO (10 wt%) nanocomposite-based PENGs.	87
Table 3.3	A detailed comparison between experimental and simulated results for earlier published works.	88

S. No.	Chapter 6	Page No.
Table 6.1	A comparison table of recently reported transferred charge density.	145